Computers & Geosciences 85 (2015) 10–21

Contents lists available at ScienceDirect

Computers & Geosciences

journal homepage: www.elsevier.com/locate/cageo

Case study

Three-dimensional wave-coupled hydrodynamics modeling in South San Francisco Bay

Yi-Ju Chou [a,b,*], Rusty C. Holleman [c], Oliver B. Fringer [e], Mark T. Stacey [d], Stephen G. Monismith [e], Jeffrey R. Koseff [e]

[a] Institute of Applied Mechanics, National Taiwan University, Taipei 106, Taiwan
[b] Taida Institute of Mathematical Sciences, National Taiwan University, Taipei 106, Taiwan
[c] Applied Ocean Physics and Engineering Department, Woods Hole Oceanography Institute, Woods Hole, MA, USA
[d] Civil and Environmental Engineering Department, University of California, Berkeley, Berkeley, CA, USA
[e] Environmental Fluid Mechanics Laboratory, Stanford University, Stanford, CA, USA

ARTICLE INFO

Article history:
Received 11 April 2015
Received in revised form
14 August 2015
Accepted 31 August 2015
Available online 3 September 2015

Keywords:
Wave–current coupling
Radiation stress
Hydrodynamics modeling

ABSTRACT

In this paper, we present a numerical model to simulate wind waves and hydrodynamics in the estuary. We employ the unstructured-grid SUNTANS model for hydrodynamics, and within this model we implement a spectral wave model which solves for transport of wave action density with the finite-volume formulation. Hydrodynamics is coupled to the wave field through the radiation stress. Based on the unstructured grid and finite-volume formulation of SUNTANS, the radiation stress is implemented in a way that directly calculates the divergence of transport of the wave-induced orbital velocity. A coupled hydrodynamics–wave simulation of San Francisco Bay is then performed. Through the input of wind forcing that is obtained from the reconstructed wind field, the model is capable of predicting wave heights that are in good agreement with the field measurements. We examine the importance of modeling sea bed dissipation in muddy shallow water environments by using a bottom friction model and a bed mud model with different mud layer thicknesses. Moreover, currents driven by wave shoaling and dissipation are investigated in the presence of abrupt bathymetric change. We find that spatially varying wave heights induced by spatially heterogeneous bottom mud dissipation produce wave-driven currents that are stronger than those induced by wave shoaling and can be of the same order as the tidal currents in shallow water.

1. Introduction

Physical processes in shallow-water estuaries are controlled by wind and tidal forcings, both of which are strong functions of complicated bottom topography and irregular shorelines. The development of a predictive model that is able to capture the interactions of these physical factors is a key element in guiding the management of estuarine water resources.

In the past few decades, numerical models have been extensively used to understand and to predict hydrodynamics in rivers and estuaries (e.g. Gessler et al., 1999; Liu et al., 2002; Lee et al., 2004; Lumborg and Pejrup, 2005). Recently, significant effort has been made to couple the wave model SWAN (Simulating Waves Nearshore, Booij et al., 1999) with various ocean circulation models to study wave–current interaction (Haas and Warner, 2009; Huang et al., 2010; Sheng et al., 2010). Haas and Warner (2009) studied wave-induced currents subject to different forcing criteria by coupling SWAN with the two-dimensional hydrodynamics model SHORECIRC and to the three-dimensional ROMS model (Shchepetkin and McWilliams, 2005). They examined the difference between the depth-averaged and depth-varied formulations. Sheng and Liu (2011) compared two different depth-varying radiation stress formulations proposed by Xia et al. (2004) and Mellor (2008) and a depth-integrated formulation by Longuet-Higgins and Stewart (1962) using CH3D-SWAN.

More recently, owing to the capability of computations on complex geometries, unstructured-grid solvers have become a popular tool to study coastal and estuarine dynamics in which highly irregular shorelines are involved. Unstructured-grid wave models have been developed for incorporation into unstructured-grid models. Examples include the wave model FVCOM-SWAVE (Qi et al., 2009) and the unstructured version of SWAN (Zijlema, 2010), which employs the vertex-based finite difference scheme. However, difficulties arise while being coupled with the hydrodynamics model because the radiation stress is always formulated

* Corresponding author at: Institute of Applied Mechanics, National Taiwan University, Taipei 10617, Taiwan.
E-mail address: yjchou@iam.ntu.edu.tw (Y.-J. Chou).

http://dx.doi.org/10.1016/j.cageo.2015.08.010
0098-3004/

in the Cartesian coordinate system. Therefore, in unstructured grids, divergence of the radiation stress is first calculated via the wave model and serves as a point forcing term for each discrete grid cell in the hydrodynamics model. Representative works include coupling between the finite-element 2D shallow-water model ADCIRC and SWAN to model hurricane waves and storm surge (Dietrich et al., 2011) and coupling between FVCOM and SWAN to study hurricane impacting the Tempa Bay (Huang et al., 2010). However, representing divergence of the radiation stress as a point source does not guarantee conservation of wave-induced momentum transport because flux inconsistency cannot be avoided (Warner et al., 2010).

In this paper we present a three-dimensional, unstructured-grid modeling framework that couples waves and currents to capture wave-coupled hydrodynamic in a complex estuarine system. Unlike the aforementioned studies that couple the existing SWAN code with a hydrodynamics solver, we develop a framework in which the wave model is coded directly into the hydrodynamic solver, thereby eliminating the need for explicit model coupling. Although additional development effort is required, this allows for more convenient model implementations in future applications. Moreover, while the spatial discretization schemes of the aforementioned vertex-based unstructured-grid wave models (Qi et al., 2009; Zijlema, 2010) are not consistent with those used in the present hydrodynamics model, the present wave model allows for the increased model efficiency since the same numerical discretizations that are employed in the hydrodynamics modeling can be employed in the wave modeling. Through use of the finite-volume formulation in both the wave model and the implementation of the radiation stresses in the hydrodynamics, the present modeling system guarantees conservation of the wave quantities and the net wave-induced momentum transport. We then carry out a numerical simulation of wind waves and tidal currents in San Francisco Bay. The model is validated through comparison with a point measurement of the wave height and surface elevation. Because the present modeling tool is applied to shallow-water estuarine environments, we also focus on modeling the sea bed dissipation mechanism. We employ the mud dissipation model that was analytically derived by Ng (2000) and use two different mud-layer thicknesses in the mud dissipation model to study its impact on the bottom friction. Wave-induced currents are examined in locations where the waves undergo significant spatial variability due to either shoaling or bottom dissipation.

2. Model formulation

2.1. Hydrodynamics

In this study we solve the wave-coupled phase-averaged primitive equations for hydrodynamics, which are given by

$$\frac{\partial u}{\partial t} + \nabla\cdot(\mathbf{u}u) - fv = -\frac{1}{\rho_0}\frac{\partial p}{\partial x} + R_x + \nabla_H\cdot(\nu_H\nabla_H u) + \frac{\partial}{\partial z}\left(\nu_V\frac{\partial u}{\partial z}\right), \tag{1}$$

$$\frac{\partial v}{\partial t} + \nabla\cdot(\mathbf{u}v) + fu = -\frac{1}{\rho_0}\frac{\partial p}{\partial y} + R_y + \nabla_H\cdot(\nu_H\nabla_H v) + \frac{\partial}{\partial z}\left(\nu_V\frac{\partial v}{\partial z}\right), \tag{2}$$

$$0 = -\frac{\partial p}{\partial z} - g\rho, \tag{3}$$

where $\mathbf{u}$ is the horizontal velocity vector and u and v are the Cartesian components in the x and y directions, respectively, p is the hydrostatic pressure that includes the barotropic and baroclinic terms, ν is the eddy-viscosity, R_x and R_y are divergence of radiation stresses in the x and y directions, respectively, and $f = 2\Omega\sin\phi$ is the Coriolis parameter in which ϕ is the latitude and Ω is the angular velocity of the earth. In Eqs. (1) and (2), subscripts H and V represent the horizontal and vertical directions, respectively. Here, following the derivation given by Mellor (2008), the phase-averaged horizontal velocity, $\mathbf{u}$, includes the low-frequency component, namely the "current" velocity, and the component that is induced by surface displacement due to waves, namely the Stokes drift. The vertical velocity w is computed via continuity

$$\nabla\cdot\mathbf{u} = 0. \tag{4}$$

The pressure p can be written as

$$p = h + r, \tag{5}$$

where $r = \frac{1}{\rho_0}\int_z^h \rho\, dz$ is the baroclinic term due to density stratification, ρ_0 is the constant reference density and $\rho_0 + \rho$ is the total density. The free-surface height h evolves according to the depth-integrated continuity equation

$$\frac{\partial h}{\partial t} + \frac{\partial}{\partial x}\left(\int_{-d}^{h} u\, dz\right) + \frac{\partial}{\partial y}\left(\int_{-d}^{h} v\, dz\right) = 0, \tag{6}$$

where d is the water depth. The density perturbation, ρ, is computed with an equation of state, which is a linear function of salinity (s) and temperature (T).

Eqs. (1)–(3) calculate quantities averaged over the wave phase, and the divergence of radiation stresses that arise as a result of the net effect of surface deformation and nonlinear transport of wave velocities are given by (Mellor, 2008)

$$R_x = \nabla_H\cdot(\widetilde{\mathbf{u}_w u_w}) + \frac{\partial}{\partial x}(-\widetilde{w}_w^2 + E_h), \tag{7}$$

$$R_y = \nabla_H\cdot(\widetilde{\mathbf{u}_w v_w}) + \frac{\partial}{\partial y}(-\widetilde{w}_w^2 + E_h), \tag{8}$$

where $\mathbf{u}_w$ is the horizontal wave velocity vector with u_w and v_w being its components in the x and y directions, respectively, and w_w is the vertical wave velocity. The tilde indicates averaging over a wave period and E_h is the potential energy due to wave-induced surface deformation $\tilde{\eta}$, which satisfies

$$E_h = 0 \quad \text{if } z \neq h \text{ and } \int_{-d}^{h} E_h\, dz = g\frac{\widetilde{\eta^2}}{2} = \frac{E}{2}, \tag{9}$$

where E is the wave energy. In Mellor (2008), it is suggested that in the finite difference formulation, only the top layer would be occupied by $1/\delta z\partial E_h/\partial x\,(\partial y)$, in which δz is the grid size. However, it has been observed that this results in a strong offshore near-surface current at the transition from the inner shelf to surf zone due to the positive gradient of cross-shore radiation stress when wave shoaling occurs (Kumar et al., 2011). In the present study, following Kumar et al. (2011), the strong offshore current is reduced by introducing a distribution function F_{ED} similar to type-III distribution function in Uchiyama et al. (2010), defined as

$$F_{ED} = \frac{FB}{\int_{-d}^{h} FB\, dz} \tag{10}$$

$$FB = \cosh\left(\frac{1}{a_b H_{rms}}(z + d)\right), \tag{11}$$

where H_{rms} is the root mean squared wave height, and a_b is a constant ($=0.1$ in the present study). The potential energy E_h in

the radiation stress formulation is thus described as

$$E_h = \frac{E}{2} F_{ED}. \tag{12}$$

However, in strong wave cases, the redistribution of the surface-stress formulation (as in Mellor, 2008) to become a surface-intensified body force (Eqs. (10)–(12)) may not sufficiently reduce the unrealistic offshore current. With this regard, we further apply the surface stress due to the gradient of E_h as a source to the transport equation of turbulence kinetic energy in the present turbulence closure model. This enhances turbulent mixing, thus effectively damping the force that drives the offshore current. Because of the periodic motion, using the wave periodic function J along with the phase angle ψ, the horizontal wave velocity can be written as (e.g. Dean and Dalrymple, 1991)

$$\mathbf{u}_w = \mathbf{u}_b J(\psi) \tag{13}$$

while the vertical wave velocity is given by

$$w_w = w_b J(\psi), \tag{14}$$

where $\mathbf{u}_b = (u_b, v_b)$ is the horizontal wave orbital velocity, and w_b is the vertical wave orbital velocity. After taking the phase average over the wave period, T, Eqs. (7) and (8) can be written as

$$R_x = \frac{1}{T}\int_0^T J^2(\psi)\, d\psi \left[\nabla_H\cdot(u_b \mathbf{u}_b) - \frac{\partial}{\partial x} w_b^2\right] + \frac{\partial}{\partial x} E_h, \tag{15}$$

$$R_y = \frac{1}{T}\int_0^T J^2(\psi)\, d\psi \left[\nabla_H\cdot(v_b \mathbf{u}_b) - \frac{\partial}{\partial y} w_b^2\right] + \frac{\partial}{\partial y} E_h, \tag{16}$$

where the leading integrals on the right-hand side of both equations determine the coefficient based on the phase function. For example, if linear wave theory is employed (i.e. $\mathbf{u}_w(x, y, z, t) = \mathbf{u}_b(x, y, z)\cos(\psi)$ and $w_w(x, y, z, t) = w_b(x, y, z)\sin(\psi)$), the integrals in Eqs. (15) and (16) give 1/2, and one general form for depth-dependent radiation stress (Mellor, 2008) is recovered.

Eqs. (1)–(6) are solved using the unstructured-grid SUNTANS model (Fringer et al., 2006). In SUNTANS, the horizontal momentum equations are solved at the vertical faces of each cell to obtain the horizontal face-normal velocity, $U = \mathbf{u}\cdot\mathbf{n}$, where $\mathbf{n}$ is the face-normal vector (Fringer et al., 2006) (see Fig. 1). In this numerical framework, the radiation stress is added to the horizontal momentum equation which is given by

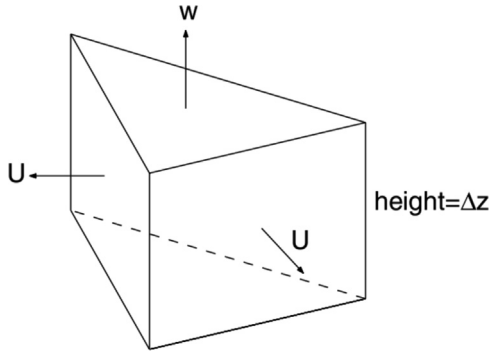

Fig. 1. Depiction of a three-dimensional prismatic grid cell in SUNTANS, showing the horizontal velocity U defined normal to the vertical cell faces (from Fringer et al., 2006).

$$\frac{\partial U}{\partial t} + \mathbf{n}\cdot\nabla\cdot(\mathbf{u}\mathbf{u}) - f\mathbf{n}\times\mathbf{u}$$

$$= -\frac{1}{\rho_0}\frac{\partial p}{\partial n} + \mathbf{n}\cdot\nabla_H\cdot(I_w \mathbf{u}_b \mathbf{u}_b) + \frac{\partial}{\partial n}(-I_w w_b^2 + E_h)$$

$$+ \mathbf{n}\cdot\nabla_H\cdot(\nu_H \nabla_H \mathbf{u}) + \frac{\partial}{\partial z}\left(\nu_V \frac{\partial U}{\partial z}\right), \tag{17}$$

where $\frac{\partial}{\partial n}$ is the face-normal gradient and I_w is the coefficient calculated from the phase integral of the square of the phase function (see Eqs. (15) and (16)). In the present study, the sinusoidal function is used as the periodic function (J) such that in Eq. (17), I_w=0.5. In Eq. (17), all terms associated with the divergence operator are calculated by integrating surface fluxes with Gauss's theorem, and the projection in the face normal direction (i.e. $\mathbf{n}\cdot$) is obtained from the two cell centers adjacent to a face, which guarantees conservation of wave-induced momentum.

The analytical form of the depth-varying formulation of the radiation stresses was first presented by Mellor (2003, 2008). When coupled with the nearshore wave model SWAN, incorporation of analytical formulation of radiation stresses into ocean circulation models allows the study of wave–current interactions in coastal regions, examples of which include ROMS (Haas and Warner, 2009), SHORECIRC (Haas and Warner, 2009), and CH3D (Sheng and Liu, 2011). In this study, rather than directly using the analytical forms, the formulation in Eq. (17) allows more flexibility to apply different wave periodic functions (wave shape). Moreover, this methodology is consistent with the unstructured-grid finite-volume formulation in SUNTANS, which allows grid adaptivity in the presence of complex bathymetry and shorelines.

2.2. Spectral wave model

As in the third generation wave model (Booij et al., 1999), the evolution of the wave spectrum is described by the balance equation of the action density spectrum $N(\sigma, \theta)$, where $N(\sigma, \theta) = E(\sigma, \theta)/\sigma$ and $E(\sigma, \theta)$ is the wave energy spectrum, σ is the relative frequency and θ is the wave propagation angle. The balance equation for $N(\sigma, \theta)$ is given by

$$\frac{\partial N}{\partial t} + \nabla_H\cdot\left[(\mathbf{c}_g + \mathbf{u})N\right] + \frac{\partial c_\sigma N}{\partial \sigma} + \frac{\partial c_\theta N}{\partial \theta} = \frac{S_{tot}}{\sigma}, \tag{18}$$

where σ is the relative radian frequency, $\mathbf{u}$ is the current velocity that is obtained from the SUNTANS hydrodynamics model, S_{tot} is the total source/sink term, θ is the wave propagation angle, $\mathbf{c}_g + \mathbf{u}$, c_σ, and c_θ are propagation speeds in geographic space ($\mathbf{c}_g$ is the group velocity), frequency space, and θ-space, respectively, and are calculated using linear wave theory (e.g. Dingemans, 1997). The total variance of the surface elevation $\langle\eta^2\rangle$ and the total energy E_{tot} are thus given by

$$\left\langle \eta^2 \right\rangle = E_{tot} = \int_0^{+\infty}\int_0^{2\pi} E(\sigma, \theta)\, d\theta\, d\sigma. \tag{19}$$

The source/sink term in Eq. (18) is composed of wind forcing, wave breaking, dissipation, and wave–wave interaction. Except the depth-induced breaking and bottom dissipation, we employ the same formulae for sink/source terms as given in SWAN. Instead of coupling SWAN with the hydrodynamics model, in the present study, Eq. (18) is solved on the unstructured grids that are also used to solved for hydrodynamics with finite-volume formulation. The details of numerical implementation and the validation of the wave model are provided in the Supplemental material.

In environments where waves are locally wind-generated such

as in San Francisco Bay, waves are mild and depth-induced breaking is rare. Therefore, for modeling depth-induced breaking, we apply the simple criterion

$$H_{Max} = B_k D, \tag{20}$$

where H_{Max} is the maximum wave height and the breaking index B_k=0.78. When the wave height exceeds its maximum value for a given depth, the wave action density is reduced to ensure that the wave height is less than or equal to H_{Max}. In the present study, seabed dissipation is a major mechanism that dissipates wave energy in shallow water. Here, it is classified as either bottom friction or mud dissipation. Details of modeling each mechanism are described below:

1. *Bottom friction*: In general, the sink term due to bottom friction can be expressed as (Collins, 1972; Madsen et al., 1988)

$$S_{bed} = -C_b \frac{\sigma^2}{g^2 \sinh^2 kD} E(\sigma, \theta) = \beta_{bed} E(\sigma, \theta), \tag{21}$$

where k is the wave number and C_b is the bottom drag coefficient that depends on the near-bottom wave orbital velocity U_{orb}. We use the formulation of Madsen et al. (1988) for C_b,

$$C_b = f_w \frac{g}{\sqrt{2}} U_{orb}, \tag{22}$$

where f_w is the friction factor estimated using the relation given in Johnsson (1988) and Madsen et al. (1988). Which can be approximated with

$$f_w = \begin{cases} 0.3 & \frac{A_b}{k_b} \le 0.2 \\ \exp\left[-8.82 + 7.02\left(\frac{A_b}{k_b}\right)^{-0.078}\right] & 0.2 < \frac{A_b}{k_b} \le 100 \\ \exp\left[-7.30 + 5.61\left(\frac{A_b}{k_b}\right)^{-0.109}\right] & \frac{A_b}{k_b} < 100, \end{cases} \tag{23}$$

where A_b is the near-bottom wave excursion amplitude that can be obtained from the wave model, and $k_b = 30 z_0$ is the equivalent Nikuradse roughness and z_0 is the equivalent log-law roughness height at which the near-bed velocity becomes zero.

2. *Mud layer:* To model the mud layer, we employ the two-layer fluid model derived by Ng (2000). This is a simplified version of the well-known model of Dalrymple and Liu (1978) who treat the mud as a highly viscous fluid. Both methods account for viscosity in the water and mud layers. However, the solution procedure of Ng (2000) does not require iteration under the assumption that the mud layer is very thin compared to the water depth.

The sink term in Eq. (18) due to wave-mud dissipation is given by (Komen et al., 1994)

$$S_{bed} = -2R_{d,m} |\mathbf{c}_g| E(\sigma, \theta), \tag{24}$$

where the dissipation coefficient is computed with

$$R_{d,m} = \frac{\delta_{s,m} k^2 r_{w/m}}{(\sinh 2kD + 2kD)} F_m^*, \tag{25}$$

and

$$F_m^* = \begin{cases} \dfrac{\sinh d_m^* \cosh d_m^* - \sin d_m^* \cos d_m^*}{\cosh^2 d_m^* \cos^2 d_m^* + \sinh^2 d_m^* \sin^2 d_m^*} & \text{if } 0 < d_m^* < 4 \\ 1 & \text{if } d_m^* \ge 4, \end{cases} \tag{26}$$

where $\delta_{s,m} = \sqrt{2\nu_m/\sigma}$ (ν_m is the mud layer viscosity) is Stokes' boundary layer thickness of the mud flow, $r_{w/m} = \rho_0/\rho_m$ is the water–mud density ratio, $D = h + d$ is the water depth, and $d_m^* = d_m/\delta_{s,m}$ is the non-dimensional depth of the mud layer normalized by the Stokes' layer thickness. The mud density, ρ_m, is defined as the density of the mixture, namely, the wet density. In terms of the dry density $\rho_{m,d}$, ρ_m can be obtained with

$$\rho_m = \rho_{m,d} + \left(1 - \frac{\rho_{m,d}}{\rho_s}\right)\rho_0, \tag{27}$$

where we assume that the sediment particle density is ρ_s = 2650 kg m^{-3}.

3. Wave-induced surface setup

Wave-induced surface setup occurs due to a divergence in wave radiation stress and is the strongest in the surf zone when waves shoal and break. When waves break, they produce a shoreward decrease in the radiation stress. Under steady state, the decrease in the radiation stress is balanced by a shoreward increase in the water level. As a result, this raises the mean elevation of the water surface above the still water level and produces a setup. Before waves break during shoaling, the balance between pressure gradient and shoreward increase of the radiation stress produces a wave setdown. Following a similar domain configuration as Sheng and Liu (2011), we carry out a simulation in a domain of size $L_x \times L_y \times L_z$ = 150 m × 50 m × 2.1 m, where L_z is the maximum water depth. The grid resolution is $N_x \times N_y \times N_z$ = 150 × 50 × 20. A linear down slope begins at the origin where the depth is 0.1 m and ends at x=80 m. The plan view of the grid and domain configuration are shown in Fig. 2. A monochromatic wave field with a period of 5 s and height 0.6 m propagates from the right to left. The breaking index is set to 0.78.

At steady state, the depth-integrated momentum balance in the absence of bottom friction is given by

$$\frac{dS_{xx}}{dx} + \rho g D \frac{dh}{dx} = 0, \tag{28}$$

where S_{xx} is the depth-integrated radiation stress. Based on linear wave theory, the analytical solution for wave setdown is given by Longuet-Higgins and Stewart (1964)

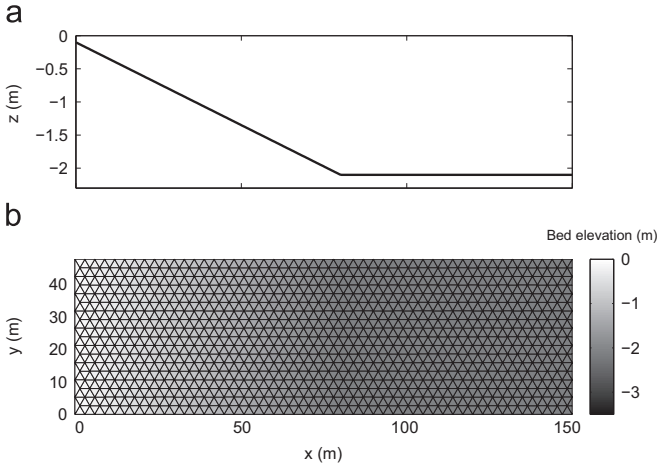

Fig. 2. Cross sectional (a) and plan (b) views of the domain used for the wave setup test case.

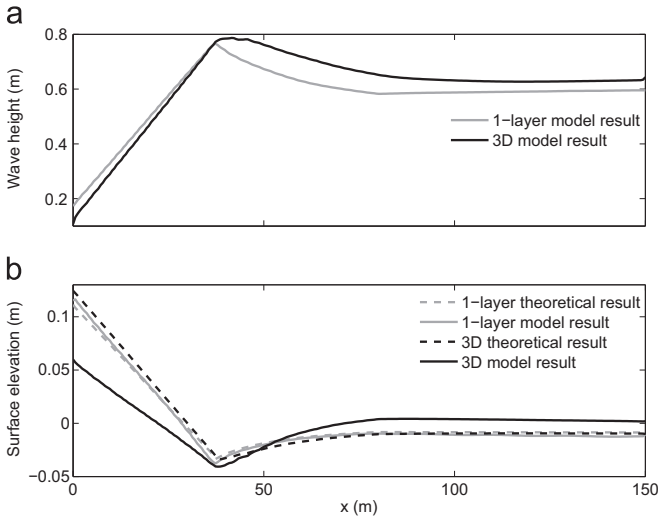

Fig. 3. Comparison between analytical and numerical solutions for the wave setup test case.

$$h = -\frac{1}{2}\frac{a^2 k}{\sinh 2kD}, \tag{29}$$

where a is the wave amplitude, and the analytical solution for wave setup is given by

$$h(x) = h_b + \frac{3B_k^2/8}{1+3B_k^2/8}[D_b - D(x)], \tag{30}$$

where h_b and D_b are the surface elevation and the water depth, respectively, when the wave starts to break. Wave setup has frequently been used to test the radiation stress in a coupled wave-current model to verify that the mean wave effect on hydrodynamics is correctly captured (e.g. Haas and Warner, 2009; Sheng and Liu, 2011). In these studies due to the direct application of the theoretical formulation, agreement with the analytical solution is guaranteed. However, it should be noted that Eq. (28) does not take the bottom friction into account. Wave shoaling produces larger waves in shallow water which produces a radiation stress gradient away from the deep water and thus drives flow from near shoal to deep water. Therefore, as the depth-integrated equation is employed, a compensated friction needs to be included to account for the bottom friction due to the return current (i.e. undertow), which is not resolved in the depth-integrated model.

The influence due to disregarding the return current in the depth-integrated model is not only seen on the resulting surface elevation, but also on the wave amplitude distribution. Fig. 3a compares the wave height distributions for a solution with 1 vertical layer (SUNTANS uses z-levels) to the solution with multiple layers, and shows that, during shoaling the 3D result gives a much more gentle increase in the wave height before breaking. This is due to a shoaling-induced offshore current (i.e. negative horizontal velocity) in the near-surface region (see Fig. 4). Moreover, Fig. 3b compares theoretical and modeled surface setup corresponding to the wave height distribution in Fig. 3a for the 1- and multi-layer results. The theoretical setup results are all calculated from the simulated wave heights in Fig. 3a using Eqs. (29) and (30). In Fig. 3b, the 1-layer model shows excellent agreement with the theoretical result while the 3D model gives an appreciable deviation from the theoretical results, which is due to the flow-induced shear stress at the bottom. This can be shown by assuming stress-free surface and deriving the depth-integrated formulation for three-dimensional momentum balance in the presence of bottom friction, which reads

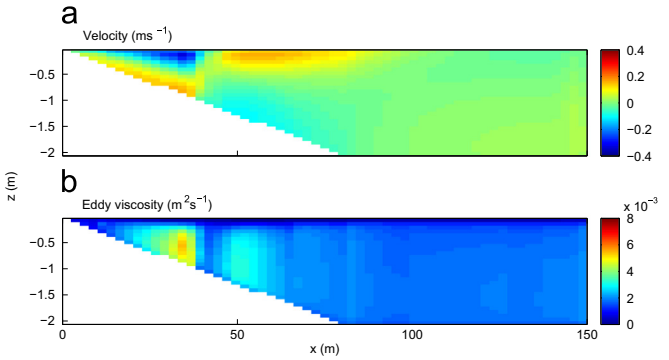

Fig. 4. Vertical profiles of the horizontal velocity (top) and eddy viscosity (bottom) along the cross-shore transect at the middle of the domain (y=25 m). In the top panel, the blue color represents the flow direction from right to left (onshore), while the red color represents the flow direction from left to right (offshore). (For interpretation of the references to color in this figure legend, the reader is referred to the web version of this article.)

$$\frac{dS_{xx}}{dx} + \rho g D\frac{dh}{dx} + \tau_B = 0, \tag{31}$$

where τ_B is the shear stress at the bottom. In SUNTANS, τ_B is given by the drag law for the bottom boundary condition for the horizontal momentum equation (Fringer et al., 2006),

$$\nu_V \frac{\partial U}{\partial z} = \frac{\tau_B}{\rho_0} = C_{d,B}|U|U, \tag{32}$$

where $C_{d,B}$ is the drag coefficient. As shown in Fig. 4a, before breaking, there is an appreciable offshore current near the surface and a weak onshore current near the bottom, resulting in a steeper slope (see Eq. (31)) than the theoretical result. On the other hand, after breaking, the offshore current at the bottom (undertow) produces a positive friction, leading to a reduction of the surface set-up in comparison to the theoretical result. Since the undertow balances the strong shoreward current driven by the shoreward decrease of the surface deformation, the abrupt vertical transition of the horizontal momentum in the breaking zone results in the strong eddy viscosity due to shear production, as shown in Fig. 4b. Therefore, a turbulence model that is able to precisely capture the unresolved turbulent effect and produce the relevant eddy-viscosity is essential. Here the MY25 turbulence model that accounts for the shear production seems to give satisfactory results. However, the development of a turbulence model that also takes the wave-breaking effect into account deserves future study.

4. San Francisco Bay simulation

4.1. Model setup

We employ the domain and setup of Chua and Fringer (2011), who model tide-driven flows and salinity transport in San Francisco Bay during January 2005 using SUNTANS. Here we summarize the important features of that model, although the reader is referred to Chua and Fringer (2011) for more detail.

The computational domain extends from the Pacific Ocean to the Sacramento-San Joaquin River Delta. This includes Central Bay, San Pablo Bay, Suisun Bay, and South Bay, as shown in Fig. 5. There are two open boundaries. One is the ocean boundary at the Pacific Ocean, which extends approximately 40 km from the Golden Gate. This distance is chosen because the northern most open boundary aligns with Point Reyes, where a tide gauge is located and used for model forcing. The other open boundary is at the Sacramento-San Joaquin Delta. The complex and interconnected network of

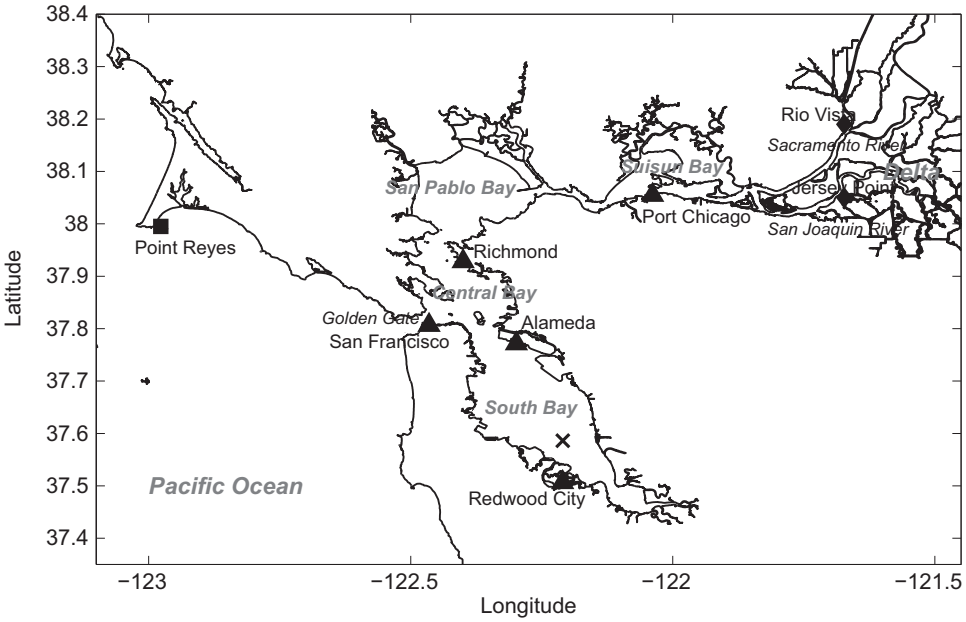

Fig. 5. Shoreline of the San Francisco Bay region showing locations of wind stations (black triangles), observations of free-surface heights (black square), and SSC and wave observations (×).

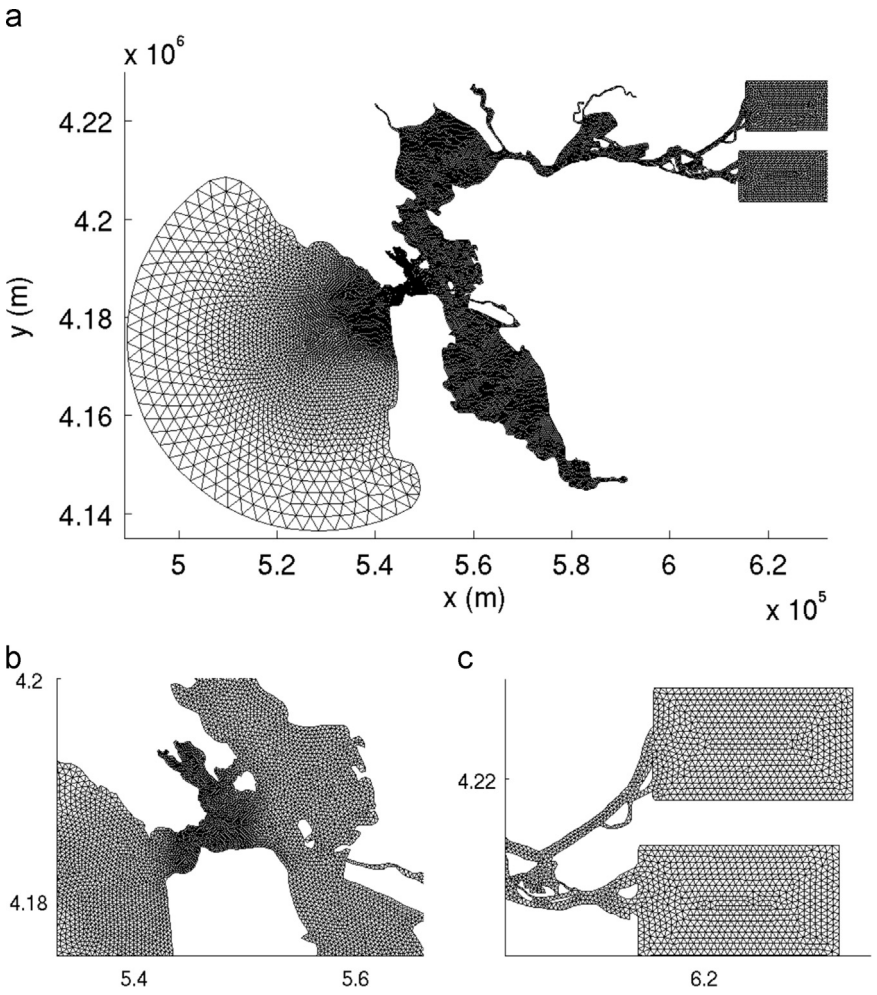

Fig. 6. Unstructured grid of the San Francisco Bay domain used in the present study, showing (a) the entire domain, (b) the Golden Gate region, and (c) the rectangular "false deltas", following Chua and Fringer (2011).

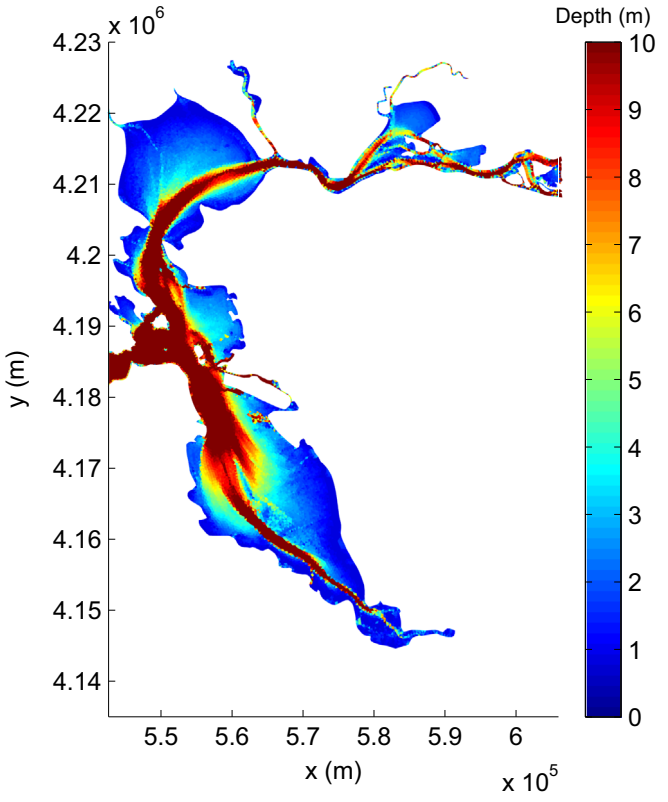

Fig. 7. San Francisco Bay bathymetry. Although the water depth ranges from 0 to 225 m in this domain, we limit the color scale to a maximum of 10 m to emphasize the shallower regions of the bay. (For interpretation of the references to color in this figure legend, the reader is referred to the web version of this article.)

tributaries in the delta is represented by a "false delta", which consists of two rectangles (Gross et al., 2005), as shown in Fig. 6. This allows specification of inflow conditions from the Delta. As shown in Fig. 7, the greatest depth in San Francisco Bay is located at the Golden Gate, which is about 110 m. There is a distinct channel that extends throughout the bay along its thalweg, and this channel incises shallow shoals. The channel depth varies from 10 m to 30 m while the shoals are usually less than 5 m deep.

The horizontal grid configuration is shown in Fig. 6. The average grid resolution based on triangular cell lengths is 50 m. In the vertical, the grid has structured z-levels, with a maximum of 60 layers in the deepest portion of the domain. With a grid stretching radio of 10% in the z-direction, the vertical resolution is refined in the upper layer, and the minimum vertical grid size is 0.29 m. The total number of cells in the horizontal is approximately 80,000 with more than 80% located in the Bay. The three-dimensional grid has approximately 2.5 million grid cells.

As discussed in Chua and Fringer (2011), hydrodynamic model stability is limited by small grid spacing and strong flows at the Golden Gate, where the Voronoi distance between adjacent cells is $\Delta x = 20$ m and the currents reach $u = 2$ m s^{-1}, thus requiring a time step of 10 s. The simulation is conducted for a 14-day period starting on 9 September 2009 following a 14-day spinup period to allow the salinity field time to adjust (see Chua and Fringer, 2011). Due to the operator-splitting method (see the supplementary material) employed for solving transport of the wave action density in the present wave model, a relatively small computational time step (compared to the unsplitting method) is required for wave modeling to eliminate the numerical instability resulting from the splitting error. In the present study, waves and hydrodynamics are updated with the same time step, and numerical instability is not found throughout the simulation. Compared to the original SUNTANS hydrodynamics computation, addition of

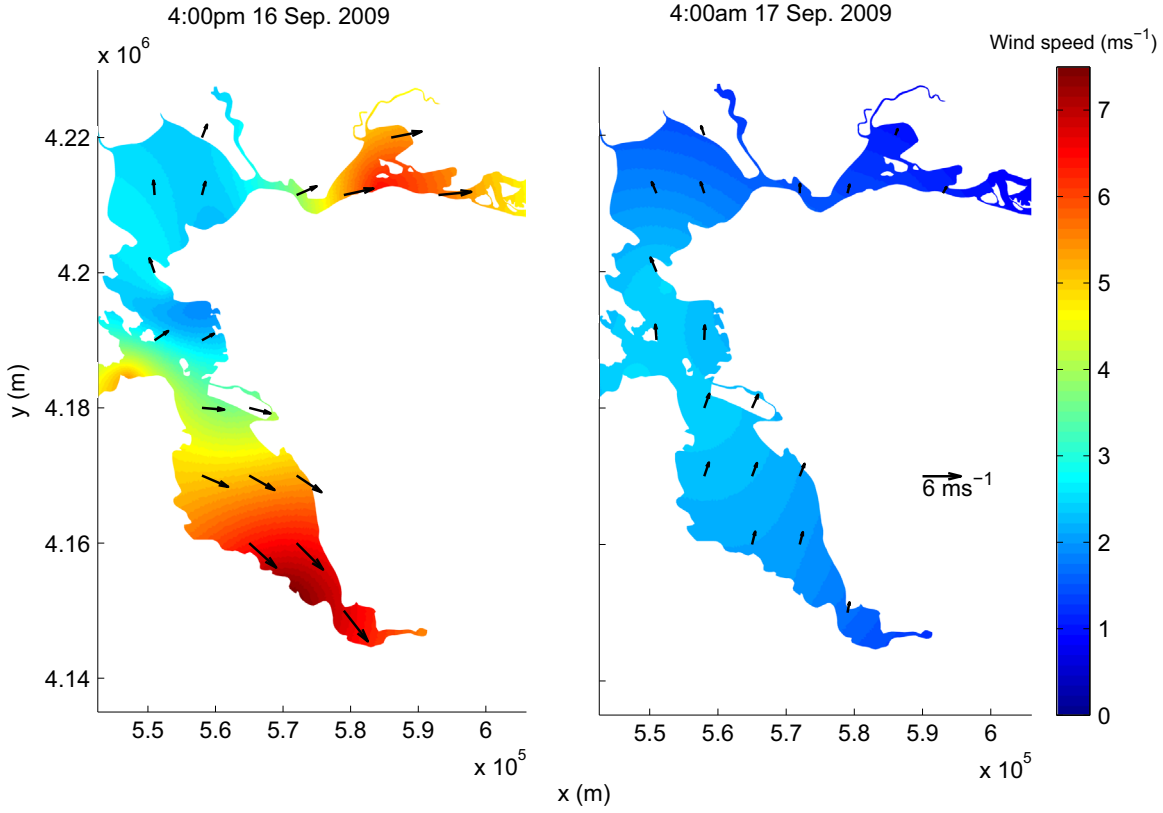

Fig. 8. Reconstructed wind speeds (colors) and wind directions (black arrows) in San Francisco Bay during a strong-wind (left) and a weak-wind period (right). (For interpretation of the references to color in this figure legend, the reader is referred to the web version of this article.)

the wave model roughly doubles the computation time. Simulation of a seven-day period requires 60,480 time steps which consumes about 10 h of wallclock time using 24 processors on the Dell PowerEdge M620 supercomputer cluster located at Taida Institute of Mathematical Sciences at National Taiwan University.

4.2. Wave model setting

Waves are modeled on the same grid as the hydrodynamics model with frequencies ranging from $0.2 \le \sigma \le 6.28$ rad s^{-1} and with the propagation angle $0 \le \theta < 360^{\circ}$. We discretize the wave action density with 36 equally spaced points in angle space and 36 logarithmically spaced points in frequency space. A mud layer with a thickness of d_m=0.2 m and viscosity=0.1 m^2 s^{-1} is used in the mud dissipation model. Another thinner mud-layer case with d_m = 0.02 m is carried out for comparison. Wind speeds and directions are reconstructed using the Kriging spatial interpolation method at each grid point using wind data from National Oceanic and Atmospheric Administration (NOAA) wind stations. There are five NOAA wind stations around the Bay, namely, San Francisco, Redwood City, Alameda, Port Chicago, and Richmond (see Fig. 5). The historical data is obtained from the NOAA National Data Buoy Center at a time resolution of 6 min. Therefore, at each simulation time step, wind data is obtained by linear interpolation from two adjacent points in the measured wind time series. Examples of the reconstructed wind field during a strong-wind and weak-wind period are shown in Fig. 8.

4.3. Results and discussion

4.3.1. Comparison to observations

Field observations were conducted in South San Francisco Bay by Brand et al. (2010) at a shallow water site (longitude: 122.20977, latitude: 37.58633, location × in Fig. 5) south of San Mateo Bridge, where the mean water depth is roughly 3 m. Another measurement with the same setup was carried out by the same research team from 24 February 2009 to 16 March 2009. Readers can refer to Brand et al. (2010), Collignon and Stacey (2012, 2013), and Lacy et al. (2014) for more detail. Comparison of modeled and observed surface elevations during the 14-day period is presented in Fig. 9, which shows that the model accurately predicts diurnal and semidiurnal tides as well as the spring-neap tidal cycle. Using the skill score (SS) defined as (Wilmott, 1981)

$$SS = 1 - \frac{\sum |X_{mod} - X_{obs}|^2}{\sum \left(|X_{mod} - \overline{X}_{obs}|^2 + |X_{obs} - \overline{X}_{obs}|^2 \right)}, \tag{33}$$

in which X_{mod} and X_{obs} are modeled and observed variables, respectively, and the overbar represents the mean value. For prediction of the surface elevation, SS=0.96. In the present simulations, the addition of the wave model does not affect the surface elevation skill score, which is expected given that the wave-induced setup and related currents are weak in the bay, although there is a persistent low-frequency response of the currents and winds (Sankaranarayanan and Fringer, 2013).

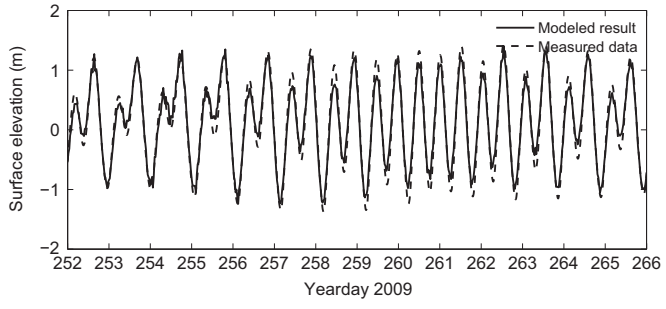

Fig. 9. Comparison of the modeled and measured surface elevation at the measurement site.

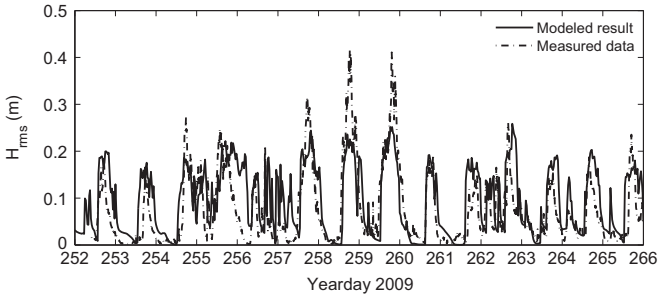

Fig. 10. Comparison of time series of the modeled and measured rms wave height (H_{rms}) at the location of the field measurements (see Fig. 5).

Comparison of time series of the rms wave height, H_{rms}, to observations is presented in Fig. 10, in which d_m=0.2 m is used as the mud layer thickness. Although there are some discrepancies in the peaks, overall the wave model prediction agrees well with the observations and the skill score for the wave model is 0.70.

4.3.2. Comparison of bed dissipation models

To understand the impact of the bottom dissipation on the wave results, we compare three bed dissipation models as described in Section 4.2. In the first two cases, we employ the mud dissipation model with a thin mud layer (d_m=0.02 m) and a thick layer (d_m=0.2 m). The case d_m=0.02 m corresponds to a case in which the mud dissipation coefficient ($R^*_{d,m}$ in Eq. (25)) is small, while the thick-mud case corresponds to the largest possible dissipation ($F^*_m = 1$). Therefore, these two cases represent extremes of bottom mud dissipation. In the third case, we use the friction model, which parameterizes friction-induced dissipation based on the wave properties and bottom roughness (see Eqs. (21)–(23)). Since the bed friction model is the original bottom dissipation model in SWAN and most wave model implementations, it is important to examine the difference between the friction model and the bed mud model. Fig. 11 shows the spatial distribution of the rms wave height for the three cases during a strong wind event at 3:00 pm on day 258 in 2009. It can be seen from Fig. 11a and b that while waves propagate towards the east and rapidly grow in amplitude during shoaling, bed mud plays a key role in dissipating wave energy in shallow water ($D < 2$ m). In the present simulation, the resulting dominant wave length ranges from 4 to 6 m such that the bottom dissipation models can only be effective when water depth is roughly equal to or less than 2 m (i.e. $\sinh(kD) < O(10)$, in Eqs. (21) and (25)). Therefore, surface gravity waves are dissipated by the bottom mud only when $D < 2$ m, where the largest difference between two mud dissipation models (d_m=0.2 and 0.02 m) is found. As shown in Fig. 11c, wave dissipation induced by bottom friction at this shallow region lies between the thick-mud and the thin-mud cases.

Both the thin-mud case (Fig. 11a) and the friction model (Fig. 11c) show relatively little bottom dissipation. Without sufficient bottom dissipation, excessive wave energy accumulates when transport of the action density encounters the shoreline leading to the development of large wave heights without significant fetch, as shown along the west coastline at the South Bay in Fig. 11a and c. In Fig. 11b, waves are not significantly impacted by wave breaking since a significant amount of wave energy is damped by bottom dissipation before the waves can reach shallow water. The lack of importance of depth-induced breaking in the presence of mud dissipation is confirmed in Fig. 12, which shows that depth-induced breaking has almost no impact on the significant wave height along transect CD in Fig. 11b with the thick

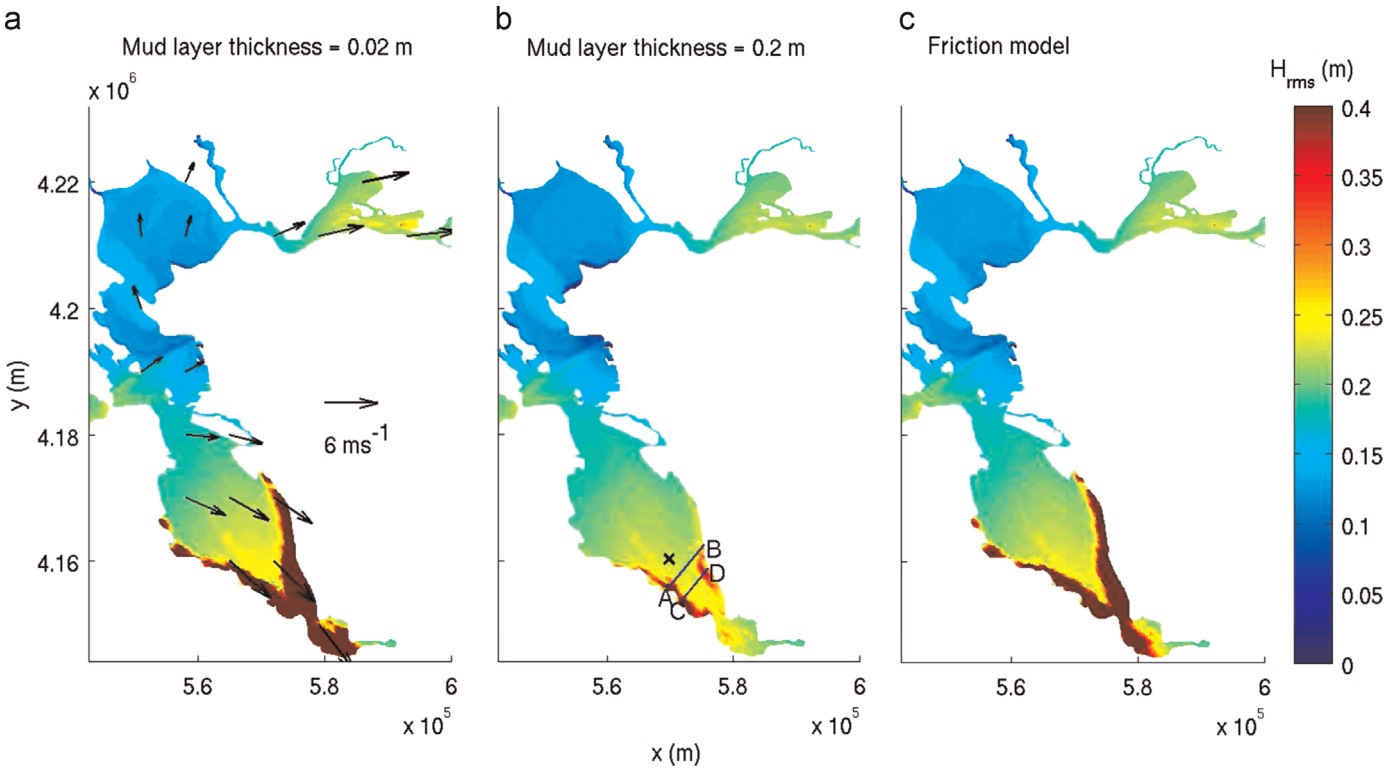

Fig. 11. Spatial distributions of the modeled H_{rms} as a result of a strong wind field at 4:00 pm on 16 September 2009 using (a) the mud dissipation model with a thin mud layer, (b) the mud dissipation model with a thick mud layer, and (c) the friction model.

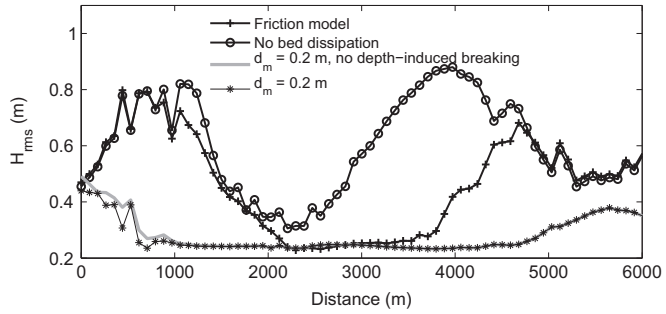

Fig. 12. Spatial distributions of the model H_{rms} along transect CD in Fig. 11b as a result of a strong wind field at 4:00 pm on 16 September 2009 using the friction model (+), only depth-induced breaking (○), the thick mud model without depth-induced breaking (gray thick line), and the thick-mud model with breaking (∗).

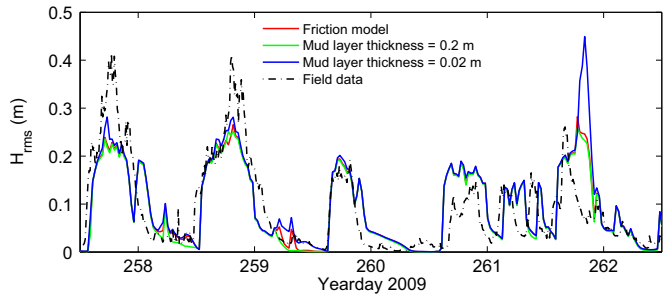

Fig. 13. Comparison of time series of the modeled and observed H_{rms} at the location of the field measurement (the × in Fig. 5) using different bed dissipation models.

mud-layer model (d_m=0.2 m). This is in contrast to what is typically seen in coastal regions where wave breaking upon shoaling is the primary damping mechanism. In the absence of mud dissipation, the controlling dissipation mechanism in shallow waters is depth-induced breaking, as shown by the similarity between the results with and without bottom friction in shallow waters in Fig. 12 (distance < 1000 m or >5000 m). The primary effect of bottom friction is to reduce the wave height in deeper water where there is no depth-induced breaking and the waves are not big enough to whitecap, as shown for 2200 m < distance < 3800 m in Fig. 12.

Time series of the rms wave height at the measurement site (the × in Fig. 11b) for the three bed dissipation cases are shown in Fig. 13, where we focus on days 257.5–262.5 which bracket two of the strongest wave events during the simulation period. The figure shows that the most significant differences among the bed dissipation models arise during peak events. As seen from Eqs. (25) and (26), given a fixed wave height, mud properties, and water depth, mud dissipation strongly depends on the mud layer thickness d_m (Eq. (26)). During peak events in the afternoon of days 257 and 258, the model with the thin mud layer gives slightly better agreement with the observations because strong wave events induce strong sediment erosion that nearly erode the top freshly deposited mud layer. As a result, the hard consolidated bed is exposed to the water column, leading to much less friction and enabling the peak wave heights seen in the observations. However, the model with the thin mud layer significantly over-predicts the wave height during the peak event on day 261, which is due to insufficient dissipation, as discussed in the previous paragraph. Another interesting but less obvious feature in Fig. 13 is that among the three different bed dissipation models, the thick mud layer gives the most dissipation during the weak wave events, resulting in the smallest rms wave height (e.g. first half of days 258 and 259). In the presence of small waves, this implies that a thick mud layer is required to provide dissipation that is sufficient to attenuate the waves. Our results suggest that wave heights are highly sensitive to the mud layer thickness and so it (or the model parameters that produce it) may be an important calibration parameter in wind-wave modeling just as the drag coefficient is in tidal modeling.

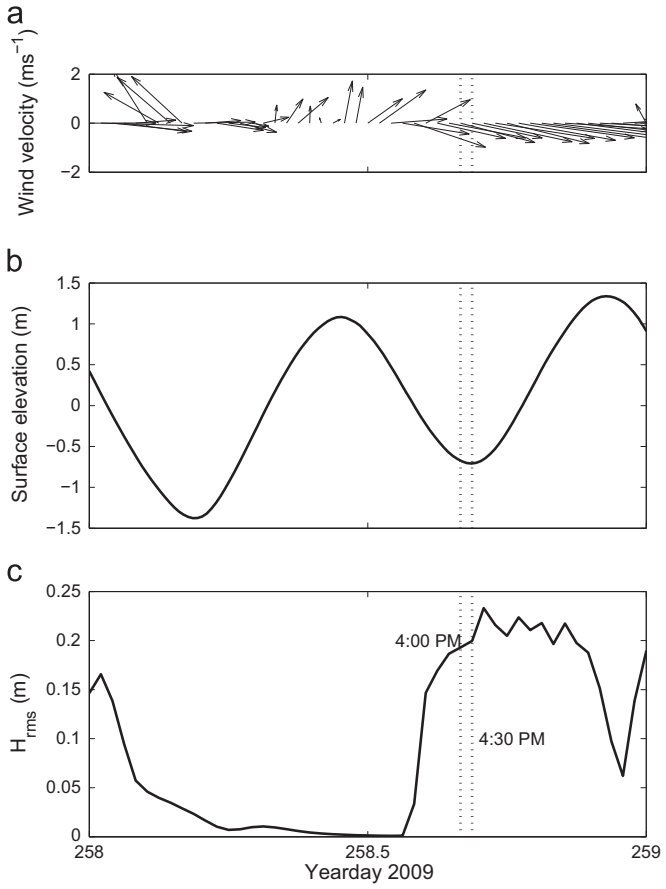

Fig. 14. Time series of (a) wind velocity, (a) the modeled surface elevation and (c) the rms wave height during day 258 highlighting (with black dotted lines) time instants corresponding to Fig. 15 (4:00 pm) and Fig. 16 (4:30 pm).

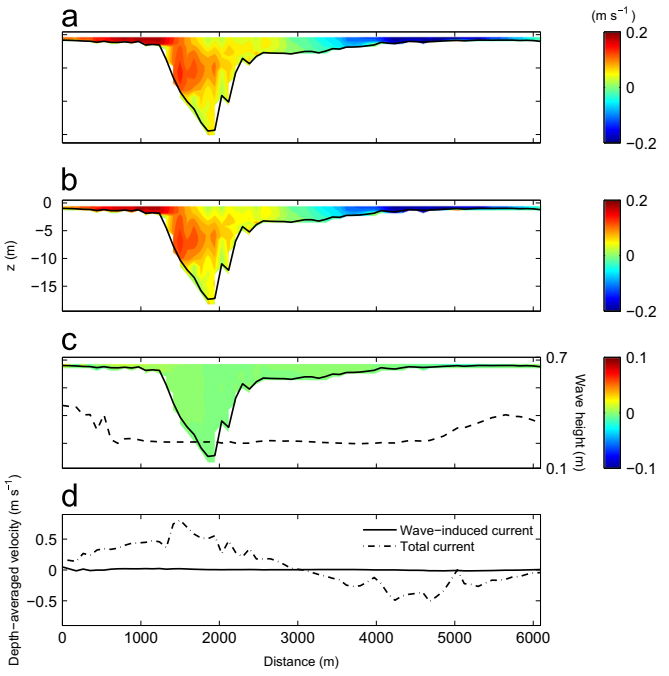

Fig. 15. Vertical profiles of the phase-averaged velocity directed along transect *CD* depicted in Fig. 11b at 4:00 pm on 16 September 2009 (a) with waves and (b) without waves. The profile in (c) shows the wave-induced along-transect currents obtained by subtracting (b) from (a). The dashed line in (c) represents the modeled wave height distribution along the transect, and the magnitude is indicated on the right *y*-axis. Note that the color axes limits in panels (a) and (b) are the same while panel (c) differs to bracket the weaker wave-driven currents. The blue color represents the flow direction from right to left, while the red color represents the flow direction from left to right. (For interpretation of the references to color in this figure legend, the reader is referred to the web version of this article.)

4.3.3. *Wave-induced currents*

Comparison of simulation results with and without the radiation stress enables the investigation of wave-induced currents. The most pronounced wave-induced currents occur at the shoal-channel transition in South San Francisco Bay, particularly during strong wind events that occur when tidal currents are weak and water depths are at their lowest during the low slack tides. Such a situation occurs around 4:00 pm on day 258 (16 September) 2009, when higher-low water (see Fig. 9) coincides with a strong wind event, as shown by the zoomed-in plots of simulated time series of the surface elevation and wave height along with the reconstructed wind velocity in Fig. 14. The corresponding spatial distribution of the RMS wave height in the bay is presented in Fig. 11b, which shows a sharp growth of the wave height in South Bay due to shoaling of waves generated by winds from the northwest as they propagate into shallow water in the shoals. Currents along the transect CD in Fig. 11b with and without waves are depicted in Fig. 15a and b, respectively. The difference between the two is an indication of the wave-driven flow as depicted in Fig. 15c, which also shows the distribution of rms wave heights along the transect. Comparison of the depth-averaged velocity between the total current and wave-driven flow along the transect is shown in Fig. 15d. As mentioned in Section 3, wave shoaling produces a radiation stress gradient away from the main channels and thus drives flow from the shoals to the channel. This is indicated by eastward flow from the western shoals roughly at 500–1200 m in Fig. 15c and westward flow from the eastern shoals roughly at 4500–5500 m in Fig. 15c. However, compared to the velocity of the overall along-transect current, such shoaling-induced current is relatively weak and is negligible at this time instant, as shown in Fig. 15d. Such a situation is quite different from that in Fig. 16, which presents the same plots as in Fig. 15 but at 30 min later. Fig. 14 shows the slight decrease of the water level from 4:00 pm in Fig. 15 to 4:30 pm in Fig. 16. The increase of wave height in the western shoal (500–1200 m in Figs. 15c and 16c) along with the slight decrease of the water level results in stronger wave dissipation caused by the bottom mud, which exhibits a relatively stronger decay in wave height, especially in the shallowest parts of the shoals during the low-water period. As shown in Fig. 16c, the wave height on the western shoals decays moving toward the shore which results in a radiation stress gradient directed offshore. This drives a shoreward current at the shoal channel transition that is much stronger than that which might be induced by wave shoaling, as compared to Fig. 15c. Fig. 16d shows that in the very shallow region at the western shoal, the magnitude of such wave-induced currents can be comparable to the tidal currents.

It can be seen from Figs. 15 and 16 that there are competing mechanisms responsible for the generation of wave-induced currents. The first mechanism is associated with growing wave height during shoaling which produces a weak current from the shoals to the channel. The second is due to wave damping induced by bottom dissipation when the water depth becomes shallower, which drives relatively stronger current towards the shoal. In the present simulation, strong damping of waves in shallow waters produces a heterogeneous wave height distribution and hence produces radiation stress gradients that drive currents which can be comparable to the tidal currents in shallow waters during the low slack tide. As shown in Fig. 16, this mechanism dominates the currents induced by shoaling waves which give rise to comparatively weaker offshore currents.

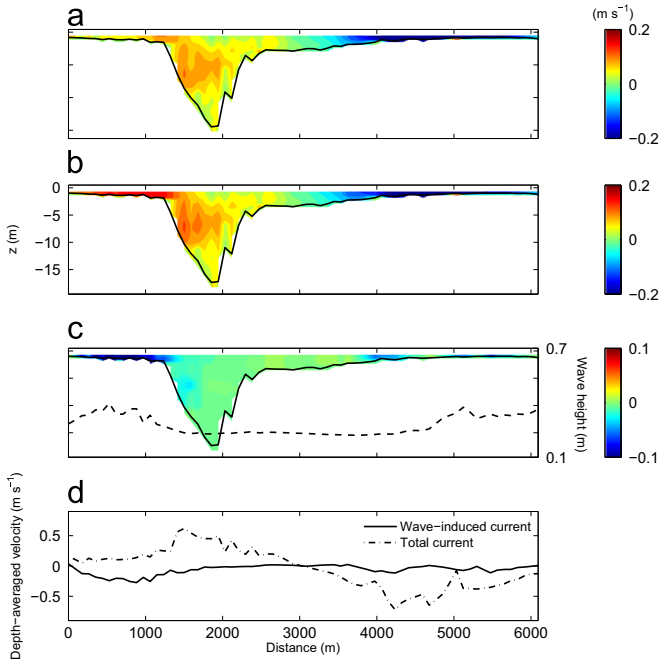

Fig. 16. Vertical profiles of the phase-averaged velocity directed along transect *CD* depicted in Fig. 11b at 4:30 pm on 16 September 2009 (a) with waves and (b) without waves. The profile in (c) shows the wave-induced along-transect currents obtained by subtracting (b) from (a). The dashed line in (c) represents the modeled wave height distribution along the transect, and the magnitude is indicated on the right *y*-axis. Note that the color axes limits in panels (a) and (b) are the same while panel (c) differs to bracket the weaker wave-driven currents. The blue color represents the flow direction from right to left, while the red color represents the flow direction from left to right. (For interpretation of the references to color in this figure legend, the reader is referred to the web version of this article.)

5. Summary and conclusions

We have presented a three-dimensional wave-coupled hydrodynamics model and applied it to understand waves and currents in South San Francisco Bay. The wave model is built upon the unstructured-grid SUNTANS hydrodynamics model that solves the primitive equations on unstructured grids using the finite-volume formulation. Our model differs from existing studies that adopt the standard analytical form of radiation stresses based on linear wave theory in that we directly calculate net wave momentum transport based on the finite-volume form of the discrete divergence of the radiation stress. This guarantees conservation of wave-induced momentum.

A simple idealized test case of wave-induced surface setup is then conducted to validate the wave-current coupling. Comparison to the analytical result shows the influence of the wave-induced current on both the wave height distribution and the resulting surface setup and setdown. We then carry out numerical simulation of waves and tides in San Francisco Bay. Comparison of the modeled surface elevation to field observations demonstrates model capability to capture the correct tidal currents. With the wind field that is reconstructed through interpolation from NOAA stations, the spectral wave model enables calculation of the phase-averaged properties of the resulting wind waves. Good agreement between the modeled wave height and the observations is obtained. A further comparison is made for different bed dissipation mechanisms. The results show that the differences are clear particularly during strong-wave periods in shallow-water regions ($d < 3$ m), indicating the importance of good parameterizations of surface wave attenuation due to the presence of bottom mud in shallow water estuarine environments. Model production of wave-induced currents is also illustrated via analysis of horizontal velocity profiles along vertical transects in South San Francisco Bay. During strong wave events approaching low tides, weak currents directed towards the channels arise from shoaling at shoal-channel transitions. However, as the water depth approaches its minimum during low tides, strong dissipation due to wave–mud interactions leads to a strong reduction in wave height moving towards the shores. This gives rise to an oppositely signed radiation stress gradient which drives a current away from the channels to the shores. Such a current induced by strongly heterogeneous bottom-mud dissipation can be of the same order of magnitude as the tidal currents and may be important for channel-shoal exchange.

Acknowledgment

The project was supported by a grant from the California Coastal Conservancy. Simulations were carried out using supercomputers at the Peter A. McCuen Environmental Computing Center at Stanford University and at Taida Institute of Mathematical Science (TIMS) at National Taiwan University.

Appendix A. Supplementary data

Supplementary data associated with this paper can be found in the online version at http://dx.doi.org/10.1016/j.cageo.2015.08.010.

References

Booij, N., Ris, R.C., Holthuijsen, L.H., 1999. A third generation wave model for coastal regions: 1. Model description and validation. J. Geophys. Res. 104 (C4), 7649–7666.
Brand, A., Lacy, J.R., Hsu, K., Hoover, D., Gladding, S., Stacey, M.T., 2010. Wind-enhanced resuspension in the shallow waters of South San Francisco bay: mechanisms and potential implications for cohesive sediment transport. J. Geophys. Res. 115, C11024.
Chua, V.P., Fringer, O.B., 2011. Sensitivity analysis of three-dimensional salinity simulations in north san francisco bay using the unstructured-grid suntans model. Ocean Model. 39, 332–350.
Collignon, A.G., Stacey, M.T., 2012. Intratidal dynamics of fronts and lateral circulation at the shoal-channel interface in a partially stratified estuary. J. Phys. Oceanogr. 42 (5), 869–883.
Collignon, A.G., Stacey, M.T., 2013. Turbulence dynamics at the shoal-channel interface in a partially stratified estuary. J. Phys. Oceanogr. 43 (5), 970–989.
Collins, J.I., 1972. Prediction of shallow water spectra. J. Geophys. Res. 77 (15), 2693–2707.
Dalrymple, R.A., Liu, P.L., 1978. Waves over soft muds: a 2-layer fluid model. J. Phys. Oceanogr. 8, 1121–1131.
Dean, R.G., Dalrymple, R.A., 1991. Water Wave Mechanics for Engineers and Scientists. Advanced Series on Ocean Engineering vol. 2. World Scientific, River Edge, NJ, p. 193.
Dietrich, J.C., Zijlema, M., Westerink, J.J., Holthuijsen, L.H., Dawson, C., Luettich Jr., R. A., Jensen, R.E., Stone, J.M., Stelling, G.S., Stone, G.W., 2011. Modeling hurricane waves and storm surge using integrally-coupled, scalable computations. Coast. Eng. 58, 45–65.
Dingemans, M.W., 1997. Water Wave Propagation Over Uneven Bottoms. Advanced Series on Ocean Engineering vol. 13. World Scientific, River Edge, NJ, p. 471.
Fringer, O.B., Gerritsen, M., Street, R.L., 2006. An unstructured-grid finite volume, nonhydrostatic, parallel coastal ocean simulator. Ocean Model. 14, 139–173.
Gessler, D., Hall, B., Spasojevic, M., Holly, F., Pourtaheri, H., Raphelt, N., 1999. Application of a 3d mobile bed, hydrodynamic model. J. Hydraul. Eng. 125 (7), 737–749.
Gross, E.S., MacWilliams, M.L., Kimmerer, W., 2005. Simulating periodic stratification in the san francisco estuary. In: Proceedings of the 9th International Conference on Estuarine and Coastal Modelling, ASCE Conference Proceedings, pp. 155–175.
Haas, K.A., Warner, J.C., 2009. Comparing a quasi-3d to a full 3d nearshore circulation model: shorecirc and roms. Ocean Model. 26, 91–103.
Huang, Y., Weisberg, R.H., Zheng, L., 2010. Coupling of surge and waves for an Ivan-like hurricane impacting the Tempa Bay, Florida region. J. Geophys. Res. 115, C12009.
Johnsson, I.G., 1988. Wave boundary layer and friction factor. in coastal engineering 1966. In: Proceedings of the 10th International Conference on Coastal

Engineering, ASCE, New York, pp. 127–148.
Komen, G.J., Cavaleri, L., Donelan, M., Hasselmann, K., Hasselmann, S., Janssen, P.A.E. M., 1994. Dynamics and Modelling of Ocean Waves. Cambridge University Press, Cambridge, p. 532.
Kumar, N., Voulgaris, G., Warner, J.C., 2011. Implementation and modification of a three-dimensional radiation stress formulation for surf zone and rip-current applications. Coast. Eng. 58, 1097–1117.
Lacy, J.R., Gladding, S., Brand, A., Collignon, A., Stacey, M., 2014. Lateral baroclinic forcing enhances sediment transport from shallows to channel in an estuary. J. Phys. Oceanogr., 1–20.
Lee, V., Mineart, P., Armstrong, L., 2004. Calibration of a sediment transport model for san francisco bay. In: Proceedings of the 8th International Conference on Estuarine and Coastal Modeling, pp. 1007–1026.
Liu, W., Hsu, M., Kuo, A.Y., 2002. Modelling of hydrodynamics and cohesive sediment transport in Tanshui river estuarine system, Taiwan. Mar. Pollut. Bull. 44, 1076–1088.
Longuet-Higgins, M.S., Stewart, R.W., 1962. Radiation stress and mass transport in gravity waves, with application to “surfbeats”. J. Fluid Mech. 13, 481–504.
Longuet-Higgins, M.S., Stewart, R.W., 1964. Radiation stress in water waves: a physical discussion and applications. Deap-Sea Res. 11, 529–562.
Lumborg, U., Pejrup, M., 2005. Modelling of cohesive sediment transport in a tidal lagoon - an annual budget. Mar. Geol. 218, 1–16.
Madsen, O.S., Poon, Y.K., Graber, H.C., 1988. Spectral wave attenuation by bottom friction: theory. in coastal engineering 1988. In: Proceedings of the 21th International Conference on Coastal Engineering, ASCE, New York, pp. 492–504.
Mellor, G.L., 2003. The three-dimensional current and surface wave equations. J. Phys. Oceanogr. 33, 1978–1989.
Mellor, G.L., 2008. The depth-dependent current and wave interaction equations: a revision. J. Phys. Oceanogr. 38, 2587–2596.
Ng, C., 2000. Water waves over a muddy bed: a two-layer Stokes' boundary layer model. Coast. Eng. 40, 221–242.
Qi, J., Chen, C., Beardsley, R.C., Perrie, W., Cowles, G.W., Lai, Z., 2009. An unstructured-grid finite-volume surface wave model (fvcom-swave): implementation, validation, and applications. Ocean Model. 28, 153–166.
Sankaranarayanan, S., Fringer, O.B., 2013. Dynamics of barotropic low-frequency fluctuations in San Francisco Bay during upwelling. Cont. Shelf Res. 65, 81–96.
Shchepetkin, A.F., McWilliams, J., 2005. The regional oceanic modeling system: a split-explicit, free-surface, topography-following-coordinate ocean model. Ocean Model. 9, 347–404.
Sheng, Y.P., Alymov, V., Paramygin, V.A., 2010. Simulation of a storm surge, wave, currents, and inundation in the outer banks and chesapeake bay during hurricane Isabel in 2003: the importance of waves. J. Geophys. Res. 115, C04008.
Sheng, Y.P., Liu, T., 2011. Three-dimensional simulation of wave-induced circulation: comparison of three radiation stress formulation. J. Geophys. Res. 116, C050521.
Uchiyama, Y., McWilliams, J.C., Shchepetkin, A.F., 2010. Wave–current interaction in an oceanic circulation model with a vortex-force formalism: application to the surf zone. Ocean Model. 34, 16–35.
Warner, J.C., Armstrong, B., He, R., Zambon, J.B., 2010. Development of a coupled ocean-atmosphere-wave-sediment transport modeling system. Ocean Model. 35, 230–244.
Wilmott, C.J., 1981. On the validation of models. Phys. Geogr. 2, 184–194.
Xia, H., Xia, Z., Zhu, L., 2004. Vertical variation in radiation stress and wave-induced currents. Coast. Eng. 51, 309–321.
Zijlema, M., 2010. Computation of wind-wave spectra in coastal waters with swan on unstructured grids. Coast. Eng. 57, 267–277.